Earth Syst. Sci. Data Discuss., 6, 779–809, 2013
www.earth-syst-sci-data-discuss.net/6/779/2013/
doi:10.5194/essdd-6-779-2013

Open Access Earth System Science Data Discussions

High resolution atmospheric reconstruction for Europe 1948–2012: coastDat2

B. Geyer

Institute of Coastal Research, Helmholtz-Zentrum Geesthacht, Geesthacht, Germany

Received: 5 November 2013 – Accepted: 18 November 2013 – Published: 2 December 2013

Correspondence to: B. Geyer (beate.geyer@hzg.de)

Published by Copernicus Publications.

Abstract

The coastDat data sets were produced to give a consistent and homogeneous database mainly for assessing weather statistics and long-term changes for Europe, especially in data sparse regions. A sequence of numerical models was employed to reconstruct all aspects of marine climate (such as storms, waves, surges etc.) over many decades. Here, we describe the atmospheric part of coastDat2 (Geyer and Rockel, 2013, doi:10.1594/WDCC/coastDat-2_COSMO-CLM). It consists of a regional climate reconstruction for entire Europe, including Baltic and North Sea and parts of the Atlantic. The simulation was done for 1948 to 2012 with a regional climate model and a horizontal grid size of 0.22° in rotated coordinates. Global reanalysis data were used as forcing and spectral nudging was applied. To meet the demands on the coastDat data set about 70 variables are stored hourly.

1 Motivation

The precursor of coastDat2, coastDat1 (Weisse et al., 2009), was widely used. About 50 % of the coastDat1 users were commercial, while 25 % were academic and another 25 % were from authorities. Applications range from assessing long-term variability and change to risk assessment and design, for example of offshore wind farms. As coastDat1 terminated in 2007, and as there were strong requests for an upgrade comprising the most recent years at higher spatial resolution, the coastDat2 effort was implemented. The here described simulation with the community model COSMO-CLM on the current super computer of the German Climate Computing Center (DKRZ) replaces the coastDat1 regional atmospheric simulation done with REMO5.0 (Feser et al., 2001; Jacob et al., 2001). For coastal areas the higher resolution is the main advantage. The overall advantage is the availability of the last 5 yr.

2 Model set up

For the reconstruction the COSMO model in CLimate Mode (COSMO-CLM) version 4.8_clm_11 (Rockel et al., 2008; Steppeler et al., 2003) was used. The COSMO model is the non-hydrostatic operational weather prediction model applied and further developed by the national weather services joined in the COnsortium for SMall scale MOdeling (COSMO). The climate mode is applied and developed by the Climate Limited-area Modelling-Community (http://www.clm-community.eu). The use of the model is well supported by the members of the community and documented mainly via the COSMO documentation.

The simulation was done on a regular grid in rotated coordinates with a rotated pole at 170.0° W and 35.0° N with a resolution of 0.22°, a time step of 150 s and hourly output. Figure 1 presents the model domain. 40 vertical levels up to 27.2 km height and 10 soil levels down to 11.5 m depth were used. Spectral Nudging after von Storch et al. (2000) was applied for large scale wind speed components in the upper levels (above 850 hPa) to enforce the observed large scale circulation. Every fifth time step in both directions the information of the 5 largest wavelength was nudged with a nudging factor of 0.5. A detailed description on the technique was provided by Müller (2003, p. 50).

Meteorological initial and boundary conditions were taken from NCEP1 reanalysis data (Kalnay et al., 1996; Kistler et al., 2001). The simulation was initialized on first of January 1948 with interpolated fields for the air temperature, zonal and meridional wind component, specific water vapor content, specific cloud water content, surface specific humidity, surface pressure, skin temperature for sea points, thickness of surface snow amount and volume fraction of soil moisture. The interpolation to the coastDat2 grid was done by the model chain part int2lm v1.9_clm5 (Schättler, 2011). The soil moisture values of the coarse NCEP-grid require more spin up time than the few days required by atmospheric fields (Denis et al., 2002). Therefore we ran the model for five years, namely 1948 to 1952, and restarted with the gained soil moisture fields.

ESSDD
6, 779–809, 2013

Figure 2 shows the development of the moisture for area means of layers 1 to 8 for the European standard evaluation areas (Rockel and Woth, 2007) adopted by Christensen and Christensen (2007, p. 22). The layers 9 to 10 are hydrologically not active and are undefined, the water draining through layer 8 was added to the runoff. Layer 7 and 8 have the same start value of 0.33 m. After 5 yr the soil moisture reached realistic values for all regions and levels, i.e., that they were not dependent any more on the initial values as they were near to equal for both simulations (5 yr spin up and coastDat2). At the lateral boundaries the relaxation scheme by Davies (1976) was applied. The affected 10 grid boxes, the sponge zone, are cut off for all time series data of the set.

Land surface processes were parameterized with the TERRA-ML scheme (Schrodin and Heise, 2001; Doms et al., 2011). For sea points the NCEP1 skin temperatures were used as lower boundary condition. Cumulus convection was parameterized using the Tiedtke scheme (Tiedtke, 1989). Clouds were determined by the prognostic variables cloud water and cloud ice. We used a 5th order Runge–Kutta time integration scheme.

The hourly output was written in netCDF following the CF-conventions 1.4 (Eaton et al., 2009). In the appendix, Table 3, all output variables are listed.

3 External data

The surface height and orographic roughness length were taken from the gtopo30 data set of the Distributed Active Archive Center (US Geological Survey, 2004), the land-sea fraction, parameters of vegetation, leaf area, root depth and lake fraction from the Global Ecosystems V2.0. The soil type was taken from the Food and Agriculture Organization of the United Nations (FAO). The climatological deep soil temperature was taken from the CRU (Climate research Unit at the University of East Anglia). To generate a file with the merged information on the model grid the so called PrEProcessor (PEP) was used. Detailed information on the data as well as the preprocessor was given by Smiatek et al. (2008).

ESSDD
6, 779–809, 2013

4 Evaluation

The evaluation was done for several parameters. The user demands are manifold, ranging from coastDat-internal forcing for the wave model via air chemistry models to research in the field of wind energy. In this paper we show data set comparisons for the most user-requested quantities: 2 m air temperature, total precipitation, wind speed, cloud cover, and height of boundary layer.

4.1 Reference data sets

The evaluation of the data set for air temperature, precipitation, wind, and cloud cover was done by using common gridded data sets: E-OBS of the ENSEMBLES project version 8.0 (van den Besselaar et al., 2011; Haylock et al., 2008), CRU version ts_3.2 (Jones and Harris, 2011), GPCC (Global Precipitation Climatology Centre) version 6 (Rudolf et al., 2010), and REGNIE from Deutscher Wetterdienst (Dietzer, 2000). For comparison of the height of boundary layer we used station data for Lindenberg, Germany (Beyrich and Leps, 2012).

4.2 Near-surface air temperature

Figure 3 shows the mean differences between the monthly means of air temperature at 2 m height of coastDat2 and eObs8.0 for 1950–2012. The eObs data were interpolated to the rotated grid of coastDat. From April to September the differences are below ±1 °C for wide areas of mid Europe. High differences with values up to −6 and +6 °C occur over Iceland and North Africa respectively. The precursor data set coastDat1 was used as forcing for biosphere models (e.g. Vetter et al., 2008; Jung et al., 2007), where the diurnal cycle has major importance. Therefore, we determined the differences of the diurnal temperature range. It was calculated as difference between daily maximum 2 m air temperature and daily minimum 2 m air temperature. The means of the monthly

ESSDD
6, 779–809, 2013

mean differences between coastDat2 and eObs8.0 for the period 1950 to 2012 are shown in Fig. 4.

There is a tendency to underestimate the diurnal temperature range for wide areas all over the year, except for the North-Africa part. The differences in the maximum 2 m air temperature are highest for April to August. In the North African part the coastDat2 temperatures are several degrees higher than the values of eObs and in the North-eastern parts of Europe they are several degrees lower than the observations (not shown). The differences between the two data sets in minimum 2 m air temperature are much smaller, with highest deviations occurring for Africa from June to August (not shown). The main source for the differences in the diurnal temperature range is the difference in maximum 2 m air temperature.

4.3 Precipitation

Figure 5 shows the mean differences between the monthly sums of total precipitation of coastDat2 and eObs8.0. Basis is the period 1950–2012, the eObs data are interpolated to the rotated grid of coastDat. As additional material we added Fig. 10, the mean differences between the monthly sums of total precipitation of coastDat2 and GPCC6, to the appendix. Basis is the period 1950–2010, the GPCC data are interpolated to the rotated grid of coastDat.

As the data sets based on observations (eObs, GPCC and CRU) differ, we calculated the mean minimal differences between CCLM and the three observational data sets and listed them as percentages in Table 1.

To summarize the information we find especially good agreement for December to May for British Islands (A1), Iberian Peninsula (A2), France (A3), the Alps (A6) and Mediterranean (A7): deviations are below 10 % of mean observational value. The main systematic negative deviations occur from June to November for Mediterranean (A7) and June to August in East-Europe (A8), while systematic highest positive deviations are found from December to March in Scandinavia (A5). Additionally, we show the monthly mean time series of the 8 regions for CCLM and for the range of all the three

ESSDD
6, 779–809, 2013

observational data sets in the appendix (sorted by season: Fig. 11a to d). As some users of our data set are interested in especially dry or wet seasons, we show absolute values.

The REGNIE data set has a very high spatial resolution of 1 km grid spacing for all over Germany. As the data are daily resolved we have the possibility of statistics on a daily basis. Figure 6 shows a histogram of area mean daily precipitation for Germany. The borders of the classes were chosen following the recommendation of the Global Precipitation Climatology Project. The shape of the REGNIE distribution function is generally well reproduced by CCLM. However, only for the two classes from 1.7 to 3 mm day^{-1} for all seasons the three data sets show the same frequencies. For all other classes no consistent statement concerning relation between the data sets is possible.

4.4 Wind

The marine near surface wind speeds were analyzed following Winterfeldt et al. (2010). Winterfeldt et al. (2010) found an added value of the regional atmospheric simulation of coastDat1, done with REMO5.0, compared to the reanalysis of NCEP with satellite data of quikScat as reference near the coasts. These findings were reproduced for the coastDat2 data set. Important for users of our wind data is the proofed good offshore quality of the surface wind data, although the Brier skill score for wide offshore fields is negative, meaning, that NCEP1 data has a higher agreement with observations than coastDat2. As shown for the precursor data set coastDat1 by Sotillo et al. (2005, Fig. 7), the quality e.g. at platform K1 is very good. Following the idea of Sotillo et al. (2005) our Fig. 7 shows the quantile-quantile plot of observation vs. model data. On the left hand side, results are for Atlantic buoy K1 (at 48.701° N, 12.401° W) and on the right hand side for Aegean Buoy Athos (at 39.97° N, 24.72° E). K1 observations were interpolated from anemometer height of 3 m to 10 m by logarithmic wind profile, where the roughness length depends via Charnock relation on the wind speed. The NCEP1 data were linearly interpolated in time to hourly values. For the Mediterranean buoy Athos

ESSDD
6, 779–809, 2013
High resolution atmospheric reconstruction: coastDat2
B. Geyer

NCEP1 data were interpolated to the measurement output interval of 3 h. The quality of the wind fields form coastDat1 and coastDat2 is comparable with the tendency of better representation of high wind speeds in coastDat2.

4.5 Total cloud cover

The comparison of the total cloud cover of coastDat2 and CRU data is shown in Fig. 8. For most of the months and most of the areas the differences are below 10 %. Highest differences occur from June to August over North Africa and March to August over Scandinavia. For almost all over the year, the differences for Greenland are high.

4.6 Height of planetary boundary layer

Observational data for the height of the boundary layer are hardly available. As this variable is especially important when the coastDat data set is used for air chemistry applications, i.e. to simulate the transport of harmful substances, we show at least a comparison for a short term period (2003–2012) at a single station (Lindenberg, WMO No. 10393, 52.21° N, 14.10° E). As the height of the boundary layer shows a strong diurnal cycle, the data set was divided into four sets depending on the start time of the soundings. The start time of the soundings is 45 to 75 min prior to the reporting time at 00:00, 06:00, 12:00, and 18:00 UTC. Therefore the corresponding values from 23:00, 05:00, 11:00, and 17:00 UTC of the simulated data were selected. The observations are flagged with quality status flags, which were derived by the use of four different methods to calculate the height of the PBL (Beyrich and Leps, 2012). From both data sets the values with observation quality flag "good" were extracted. For comparison both values were related to ground height, because real elevation is 112 m while the model height is 63 m.

Figure 9 shows the frequency distribution of boundary layer heights from model and observation by launch time and season. The classes refer to the model levels.

ESSDD

6, 779–809, 2013

Both frequency distributions show the shift to higher values during noon for all seasons. In general the accordance of the distributions is highest for the noon soundings. The tendency to wider spread distributions at 18:00 is given for both data sets. Most of the 16 distribution functions of simulated values show a bimodal shape while the observed values functions have clear maxima, for non-noon soundings mostly beneath 213 m. The simulated frequencies in the lowest 5 model levels (in the height of 213 m) are clearly lower than the observations.

In Table 2 the numbers of good-flagged deduced heights of PBL are listed per season and sounding time, and the according medians of these and the simulated heights, and the differences of these values are also shown.

All midnight to noon simulated median values are higher than the observed within a range of 90 to 260 m. Only the autumn 06:00 UTC simulated value is less than the observed one.

5 Conclusions

To our knowledge, the data set described represents the longest regional reconstruction based on global atmospheric reanalyses at such a high spatial and temporal detail. It covers more than 60 yr and shows good agreement with observations, although there are regions where better performance would be desirable. The comparison of the variables near surface air temperature, diurnal temperature range, precipitation, cloud cover, near surface wind speed and height of PBL with observations indicate on exemplary the quality of the data set. The main advantages of the dataset are the huge number of available variables for whole Europe and the inclosure of the recent years.

Acknowledgements. The CCLM is the community model of the German climate research (www.clm-community.eu). The German Climate Computing Center (DKRZ) provided the computer hardware for the Limited Area Modelling simulations in the project “Regional Atmospheric Modelling”. The NCEP/NCAR1 reanalysis data was provided by the National Center for Atmospheric Research (NCAR). Thanks to the ENSEMBLES group updating the eObs data set according to newest findings, to the CRU crew providing the CRU time series, GPCC and DWD for allowing us to use their data. We thank the UK Met office for providing the wind measurements at Buoy K1 station number 62029. The Athos buoy data are available via the POSEIDON Operational Oceanography System, Hellenic Centre for Marine Research (www.poseidon.hcmr.gr). We thank Frank Beyrich for providing height of boundary layer data from Deutscher Wetterdienst for Lindenberg. Additionally we want to thank the providers of the external datasets (cited in detail by Smiatek et al., 2008): the FAO for soiltypes data, and USGS for the orography, and Global ecosystem data.

References

Beyrich, F. and Leps, J.: An operational mixing height data set from routine radiosoundings at Lindenberg: methodology, Meteorol. Z., 21, 337–348, doi:10.1127/0941-2948/2012/0333, 2012. 783, 786

Christensen, J. and Christensen, O.: A summary of the PRUDENCE model projections of changes in European climate by the end of this century, Climatic Change, 81, 7–30, doi:10.1007/s10584-006-9210-7, 2007. 782

Davies, H. C.: A lateral boundary formulation for multi-level prediction models, Q. J. Roy. Meteor. Soc., 102, 405–418, doi:10.1002/qj.49710243210, 1976. 782

Denis, B., Laprise, R., Caya, D., and Cote, J.: Downscaling ability of one-way nested regional climate models: the Big-Brother Experiment, Clim. Dynam., 18, 627–646, doi:10.1007/s00382-001-0201-0, 2002. 781

Dietzer, B.: Berechnung von Gebietsniederschlagshöhen nach dem Verfahren REGNIE, Deutscher Wetterdienst – Hydrometeorologie, Offenbach, 2000. 783

Doms, G. J. F., Heise, E., Herzog, H.-J., Mrionow, D., Raschendorfer, M., Reinhart, T., Ritter, B., Schrodin, R., Schulz, J.-P., and Vogel, G.: A Description of the Nonhydrostatic Regional COSMO Model, Part II: Physical Parameterization, Tech. rep., Deutscher Wetterdienst, available at: http://www.cosmo-model.org/content/model/documentation/core/cosmoPhysParamtr.pdf, 2011. 782

Eaton, B., Gregory, J., Drach, B., Taylor, K., and Hankin, S.: NetCDF Climate and Forecast (CF) Metadata Conventions, Version 1.4, available at: http://cf-pcmdi.llnl.gov/documents/cf-conventions/1.4/cf-conventions.pdf, 2009. 782

ESSDD
6, 779–809, 2013

Feser, F., Weisse, R., and von Storch, H.: Multi-decadal atmospheric modeling for Europe yields multi-purpose data, EOS Trans., 82, 305–310, doi:10.1029/01EO00176, 2001. 780

Geyer, B. and Rockel, B.: coastDat-2 COSMO-CLM, World Data Center for Climate, CERA-DB “coastDat-2_COSMO-CLM”, available at: http://cera-www.dkrz.de/WDCC/ui/Compact.jsp?acronym=coastDat-2_COSMO-CLM, 2013. 780, 794

Haylock, M. R., Hofstra, N., Tank, A. M. G. K., Klok, E. J., Jones, P. D., and New, M.: A European daily high-resolution gridded data set of surface temperature and precipitation for 1950–2006, J. Geophys. Res., 113, D20119, doi:10.1029/2008JD010201, 2008. 783

Jacob, D., Hurk, B. J. J. v. d., Andræ, U., Elgered, G., Fortelius, C., Graham, L. P., Jackson, S. D., Karstens, U., Köpken, C., Lindau, R., Podzun, R., Rockel, B., Rubel, F., Sass, B. H., Smith, R. N. B., and Yang, X.: A comprehensive model inter-comparison study investigating the water budget during the BALTEX-PIDCAP period, Meteorol. Atmos. Phys., 77, 19–44, 2001. 780

Jones, P. and Harris, I.: CRU Time Series (TS) high resolution gridded data version 3.10, NCAS British Atmospheric Data Centre, 2011. 783

Jung, M., Vetter, M., Herold, M., Churkina, G., Reichstein, M., Zaehle, S., Cias, P., Viovy, N., Bondeau, A., Chen, Y., Trusilova, K., Feser, F., and Heimann, M.: Uncertainties of modeling gross primary productivity over Europe: A systematic study on the effects of using different drivers and terrestrial biosphere models, Global Biogeochem. Cy., 21, GB4021, doi:10.1029/2006GB002915, 2007. 783

Kalnay, E., Kanamitsu, M., Kistler, R., Collins, W., Deaven, D., Gandin, L., Iredell, M., Saha, S., White, G., Woollen, J., Zhu, Y., Chelliah, M., Ebisuzaki, W., Higgins, W., Janowiak, J., Mo, K. C., Ropelewski, C., Wang, J., Leetmaa, A., Reynolds, R., Jenne, R., and Joseph, D.: The NCEP/NCAR 40-year reanalysis project, B. Am. Meteorol. Soc., 77, 437–471, 1996. 781

Kistler, R., Kalnay, E., Collins, W., Saha, S., White, G., Woollen, J., Chelliah, M., Ebisuzaki, W., Kanamitsu, M., Kousky, V., van den Dool, H., Jenne, R., and Fiorino, M.: The NCEP-NCAR 50-year reanalysis: monthly means CD-ROM and documentation, B. Am. Meteorol. Soc., 82, 247–267, 2001. 781

Müller, B.: Eine regionale Klimasimulation für Europa zur Zeit des späten Maunder-Minimums 1675–1705, Ph.D. thesis, University of Hamburg, Hamburg, available at: http://www.hzg.de/imperia/md/content/gkss/zentrale_einrichtungen/bibliothek/berichte/gkss_2004_2.pdf, 2003. 781

ESSDD
6, 779–809, 2013

High resolution atmospheric reconstruction: coastDat2

B. Geyer

Rockel, B. and Woth, K.: Extremes of near-surface wind speed over Europe and their future changes as estimated from an ensemble of RCM simulations, Climatic Change, 81, 267–280, 2007. 782, 796
Rockel, B., Will, A., and Hense, A.: The Regional Climate Model COSMO-CLM (CCLM), Meteorol. Z., 17, 347–348, 2008. 781
Rudolf, B., Becker, A., Schneider, U., Meyer-Christoffer, A., and Ziese, M.: GPCC Status Report December 2010 (On the most recent gridded global data set issued in fall 2010 by the Global Precipitation Climatology Centre (GPCC)), GPCC Status Report, available at: http://gpcc.dwd.de, 2010. 783
Schättler, U.: A Description of the Nonhydrostatic Regional COSMO-Model Part V: Preprocessing: Initial and Boundary Data for the COSMO-Model, Tech. rep., Deutscher Wetterdienst, available at: http://www.cosmo-model.org/content/model/documentation/core/cosmoInt2lm.pdf, 2011. 781
Schrodin, R. and Heise, E.: The multi-layer-version of the DWD soil model TERRA/LM, Consortium for Small-Scale Modelling (COSMO) Tech. Rep, 2, 16, 2001. 782
Smiatek, G., Rockel, B., and Schättler, U.: Time invariant data preprocessor for the climate version of the COSMO model (COSMO-CLM), Meteorol. Z., 17, 395–405, 2008. 782, 788
Sotillo, M. G., Ratsimandresy, A. W., Carretero, J. C., Bentamy, A., Valero, F., and Gonzaález Rouco, F.: A high-resolution 44-year atmospheric hindcast for the Mediterranean Basin: contribution to the regional improvement of global reanalysis, Clim. Dynam., 25, 219–236, doi:10.1007/s00382-005-0030-7, 2005. 785
Steppeler, J., Doms, G., Schättler, U., Bitzer, H., Gassmann, A., Damrath, U., and Gregoric, G.: Meso-gamma scale forecasts using the nonhydrostatic model LM, Meteorol. Atmos. Phys., 82, 75–96, doi:10.1007/s00703-001-0592-9, 2003. 781
Tiedtke, M.: A comprehensive mass flux scheme for cumulus parameterization in large-scale models, Mon. Weather Rev., 117, 1779–1800, 1989. 782
US Geological Survey: Global Digital Elevation Model (GTOPO30), Tech. rep., EROS Data Center Distributed Active Archive Center (EDC DAAC), 2004. 782
van den Besselaar, E. J. M., Haylock, M. R., van der Schrier, G., and Tank, A. M. G. K.: A European daily high-resolution observational gridded data set of sea level pressure, J. Geophys. Res., 116, D11110, doi:10.1029/2010JD015468, 2011. 783
Vetter, M., Churkina, G., Jung, M., Reichstein, M., Zaehle, S., Bondeau, A., Chen, Y., Ciais, P., Feser, F., Freibauer, A., Geyer, R., Jones, C., Papale, D., Tenhunen, J., Tomelleri, E.,

Trusilova, K., Viovy, N., and Heimann, M.: Analyzing the causes and spatial pattern of the European 2003 carbon flux anomaly using seven models, Biogeosciences, 5, 561–583, doi:10.5194/bg-5-561-2008, 2008. 783

von Storch, H., Langenberg, H., and Feser, F.: A spectral nudging technique for dynamical downscaling purposes, Mon. Weather Rev., 128, 3664–3673, 2000. 781

Weisse, R., von Storch, H., Callies, U., Chrastansky, A., Feser, F., Grabemann, I., Günther, H., Winterfeldt, J., Woth, K., and Pluess, A.: Regional meteorological-marine reanalyses and climate change projections, B. Am. Meteorol. Soc., 90, 849–860, doi:10.1175/2008BAMS2713.1, 2009. 780

Winterfeldt, J., Geyer, B., and Weisse, R.: Using QuikSCAT in the added value assessment of dynamically downscaled wind speed, Int. J. Climatol., 31, 1028–1039, doi:10.1002/joc.2105, 2010. 785

Discussion Paper | Discussion Paper | Discussion Paper | Discussion Paper |

ESSDD

6, 779–809, 2013

High resolution atmospheric reconstruction: coastDat2

B. Geyer

Table 1. Seasonal-mean minimal differences of precipitation [%] over land between CCLM and the ensemble of the three observational data (eObs, CRU, GPCC) for 1950–2010 and the 8 European sub-regions of Fig. 1: British Islands (A1), Iberian Peninsula (A2), France (A3), Mid-Europe (A4), Scandinavia (A5), Alps (A6), Mediterranean (A7), East-Europe (A8).

	A1	A2	A3	A4	A5	A6	A7	A8
DJF	**−1.2**	**3.9**	**6.4**	15	20	**7.8**	**−0.3**	24
MAM	**2.1**	**0.2**	**1.1**	**7.7**	43	**9.5**	**−1.8**	11
JJA	**−9.6**	−34	−29	−23	**2.1**	−17	−42	−33
SON	**−9.4**	−17	−14	**−6.7**	**7.0**	−14	−23	−16

ESSDD
6, 779–809, 2013

Table 2. Statistical parameters of comparison between observed and simulated PBL height, split for sounding times in column 3 to 6, and seasons in rows according to the abbreviation in column 2. Listed are the number and the median of used observed values (median O), median of simulated values (median S), and the differences of the medians. Unit of the last three variables is m.

		00:00	06:00	12:00	18:00
number	DJF	490	647	678	598
	MAM	486	630	665	633
	JJA	574	700	690	641
	SON	424	396	505	509
median O	DJF	220	136	98	127
	MAM	202	136	125	124
	JJA	384	1166	1310	661
	SON	232	829	917	109
median S	DJF	356	258	258	258
	MAM	356	258	258	258
	JJA	475	1409	1669	964
	SON	356	778	1174	258
difference	DJF	136	122	160	131
	MAM	154	122	133	134
	JJA	91	243	359	303
	SON	124	−51	257	149

ESSDD
6, 779–809, 2013

Table 3. List of output variables of coastDat2 data set. The time series's published by Geyer and Rockel (2013) are marked in column "ts" with a cross. Time independent variables are labeled with "f" and were merged in the file coastDat2_COSMO-CLM_fx.

	variable name	unit	long name	standard name	ts/fix
1	AEVAP_S	$kg\,m^{-2}$	surface evaporation	water_evaporation_amount	×
2	ALB_RAD	1	surface albedo	surface_albedo	×
3	ALHFL_S	$W\,m^{-2}$	av. surface latent heat flux	surface_downward_latent_heat_flux	×
4	ALWD_S	$W\,m^{-2}$	downward longwave radiation at the surface	–	×
5	ALWU_S	$W\,m^{-2}$	upward longwave radiation at the surface	–	×
6	APAB_S	$W\,m^{-2}$	av. surface photosynthetic active radiation	surface_downwelling_photosynthetic _radiative_flux_in_air	×
7	ASHFL_S	$W\,m^{-2}$	av. surface sensible heat flux	surface_downward_sensible_heat_flux	×
8	ASOB_S	$W\,m^{-2}$	av. surface net downward shortwave radiation	surface_net_downward_shortwave_flux	×
9	ASOB_T	$W\,m^{-2}$	av. TOA net downward shortwave radiation	net_downward_shortwave_flux_in_air	×
10	ASOD_T	$W\,m^{-2}$	av. solar downward radiation at top	–	×
11	ASWDIFD_S	$W\,m^{-2}$	diffuse downward sw radiation at the surface	–	×
12	ASWDIFU_S	$W\,m^{-2}$	diffuse upward sw radiation at the surface	–	×
13	ASWDIR_S	$W\,m^{-2}$	direct downward sw radiation at the surface	–	×
14	ATHB_S	$W\,m^{-2}$	av. surface net downward longwave radiation	surface_net_downward_longwave_flux	×
15	ATHB_T	$W\,m^{-2}$	av. TOA outgoing longwave radiation	net_downward_longwave_flux_in_air	×
16	AUMFL_S	Pa	av. eastward stress	surface_downward_eastward_stress	×
17	AVMFL_S	Pa	av. northward stress	surface_downward_northward_stress	×
18	CAPE_CON	$J\,kg^{-1}$	specific convectively avail. potential energy	atmosphere_specific_convective_available _potential_energy	×
19	CLCH	1	high cloud cover	cloud_area_fraction_in_atmosphere_layer	
20	CLCL	1	low cloud cover	cloud_area_fraction_in_atmosphere_layer	
21	CLCM	1	medium cloud cover	cloud_area_fraction_in_atmosphere_layer	
22	CLCT	1	total cloud cover	cloud_area_fraction	×
23	DURSUN	s	duration of sunshine	duration_of_sunshine	×
24	FC	s^{-1}	coriolis parameter	coriolis_parameter	f
25	FIS	$m^2\,s^{-2}$	surface geopotential	surface_geopotential	f
26	FOR_D	–	ground fraction covered by deciduous forest	–	f
27	FOR_E	–	ground fraction covered by evergreen forest	–	f
28	FR_LAND	1	land-sea fraction	land_area_fraction	f
29	H_SNOW	m	thickness of snow	surface_snow_thickness	×
30	HBAS_CON	m	height of convective cloud base	convective_cloud_base_altitude	
31	HHL	m	height	altitude	f
32	HMO3	Pa	air pressure at ozone maximum	air_pressure	
33	HPBL	m	Height of boundary layer	–	×
34	HSURF	m	surface height	surface_altitude	f
35	HTOP_CON	m	height of convective cloud top	convective_cloud_top_altitude	
36	HZEROCL	m	height of freezing level	freezing_level_altitude	
37	LAI	1	leaf area index	leaf_area_index	
38	MFLX_CON	$kg\,m^{-2}\,s^{-1}$	convective mass flux density	atmosphere_convective_mass_fluxx	
39	P	Pa	pressure	air_pressure	
40	PLCOV	1	vegetation area fraction	vegetation_area_fraction	
41	PMSL	Pa	mean sea level pressure	air_pressure_at_sea_level	×
42	PP	Pa	deviation from reference pressure	difference_of_air_pressure_from_model _reference	
43	PS	Pa	surface pressure	surface_air_pressure	×
44	QC	$kg\,kg^{-1}$	specific cloud liquid water content	mass_fraction_of_cloud_liquid_water_in_air	
45	QI	$kg\,kg^{-1}$	specific cloud ice content	mass_fraction_of_cloud_ice_in_air	
46	QR	$kg\,kg^{-1}$	specific rain content	mass_fraction_of_rain_in_air	
47	QS	$kg\,kg^{-1}$	specific snow content	mass_fraction_of_snow_in_air	
48	QV	$kg\,kg^{-1}$	specific humidity	specific_humidity	
49	QV_2M	$kg\,kg^{-1}$	2 m specific humidity	specific_humidity	×
50	QV_S	$kg\,kg^{-1}$	surface specific humidity	surface_specific_humidity	

Table 3. Continued.

	variable name	unit	long name	standard name	ts/fix
51	RAIN_CON	kg m^{-2}	convective rainfall	convective_rainfall_amount	×
52	RAIN_GSP	kg m^{-2}	large scale rainfall	large_scale_rainfall_amount	×
53	RELHUM_2M	%	2 m relative humidity	relative_humidity	×
54	RLAT	°	latitude	latitude	
55	RLON	°	longitude	longitude	
56	ROOTDP	m	root depth	root_depth	
57	RUNOFF_G	kg m^{-2}	subsurface runoff	subsurface_runoff_amount	×
58	RUNOFF_S	kg m^{-2}	surface runoff	surface_runoff_amount	×
59	SNOW_CON	kg m^{-2}	convective snowfall	convective_snowfall_amount	×
60	SNOW_GSP	kg m^{-2}	large scale snowfall	large_scale_snowfall_amount	×
61	SNOWLMT	m	height of the snow fall limit in m a.s.l.	altitude	
62	SOBS_RAD	W m^{-2}	surface net downward shortwave radiation	surface_net_downward_shortwave_flux	
63	SOILTYP	1	soil type	soil_type	f
64	SSO_GAMMA	–	anisotropy of sub-grid scale orography	–	f
65	SSO_SIGMA	–	mean slope of sub-grid scale orography	–	f
66	SSO_THETA	°	angle between principal axis of orography and east	–	
67	T	K	temperature	air_temperature	
68	T_2M	K	2 m temperature	air_temperature	×
69	T_2M_AV	K	2 m temperature	air_temperature	×
70	T_G	K	grid mean surface temperature	surface_temperature	
71	T_S	K	soil surface temperature	–	×
72	T_SNOW	K	snow surface temperature	surface_temperature_where_snow	
73	T_SO	K	soil temperature	soil_temperature	
74	TD_2M	K	2 m dew point temperature	dew_point_temperature	×
75	TD_2M_AV	K	2 m dew point temperature	dew_point_temperature	×
76	TDIV_HUM	kg m^{-2}	atmosphere water divergence	change_over_time_in_atmospheric_water _content_due_to_advection	
77	THBS_RAD	W m^{-2}	surface net downward longwave radiation	surface_net_downward_longwave_flux	
78	TKE_CON	J kg^{-1}	convective turbulent kinetic energy	–	
79	TMAX_2M	K	2 m maximum temperature	air_temperature	×
80	TMIN_2M	K	2 m minimum temperature	air_temperature	×
81	TOT_PREC	kg m^{-2}	total precipitation amount	precipitation_amount	×
82	TOT_SNOW	kg m^{-2}	total snow amount	snow_amount	×
83	TQC	kg m^{-2}	vertical integrated cloud water	atmosphere_cloud_liquid_water_content	×
84	TQI	kg m^{-2}	vertical integrated cloud ice	atmosphere_cloud_ice_content	×
85	TQV	kg m^{-2}	precipitable water	atmosphere_water_vapor_content	×
86	TWATER	kg m^{-2}	total water content	atmosphere_water_content	×
87	U	m s^{-1}	U-component of wind	grid_eastward_wind	
88	U_10M	m s^{-1}	U-component of 10 m wind	grid_eastward_wind	×
89	V	m s^{-1}	V-component of wind	grid_northward_wind	
90	V_10M	m s^{-1}	V-component of 10 m wind	grid_northward_wind	×
91	UVlat_10M	m s^{-1}	U and V-component of 10 m wind		×
92	VGUST_CON	m s^{-1}	maximum 10 m convective gust	wind_speed_of_gust	×
93	VGUST_DYN	m s^{-1}	maximum 10 m dynamical gust	wind_speed_of_gust	×
94	VIO3	Pa	vertical integrated ozone amount	equivalent_pressure_of_atmosphere_ozone _content	
95	VMAX_10M	m s^{-1}	maximum 10 m wind speed	wind_speed_of_gust	×
96	W	m s^{-1}	vertical wind velocity	upward_air_velocity	
97	W_I	m	canopy water amount	canopy_water_amount	
98	W_SNOW	m	surface snow amount	lwe_thickness_of_surface_snow_amount	
99	W_SO	m	soil water content	lwe_thickness_of_moisture_content_of _soil_layer	×
100	W_SO_ICE	m	soil frozen water content	lwe_thickness_of_frozen_water_content_of _soil_layer	×
101	WDIRlat_10M	°			×
102	WSS_10M	m s^{-1}		wind_speed	×
103	Z0	m	surface roughness length	surface_roughness_length	×

ESSDD
6, 779–809, 2013

High resolution atmospheric reconstruction: coastDat2

B. Geyer

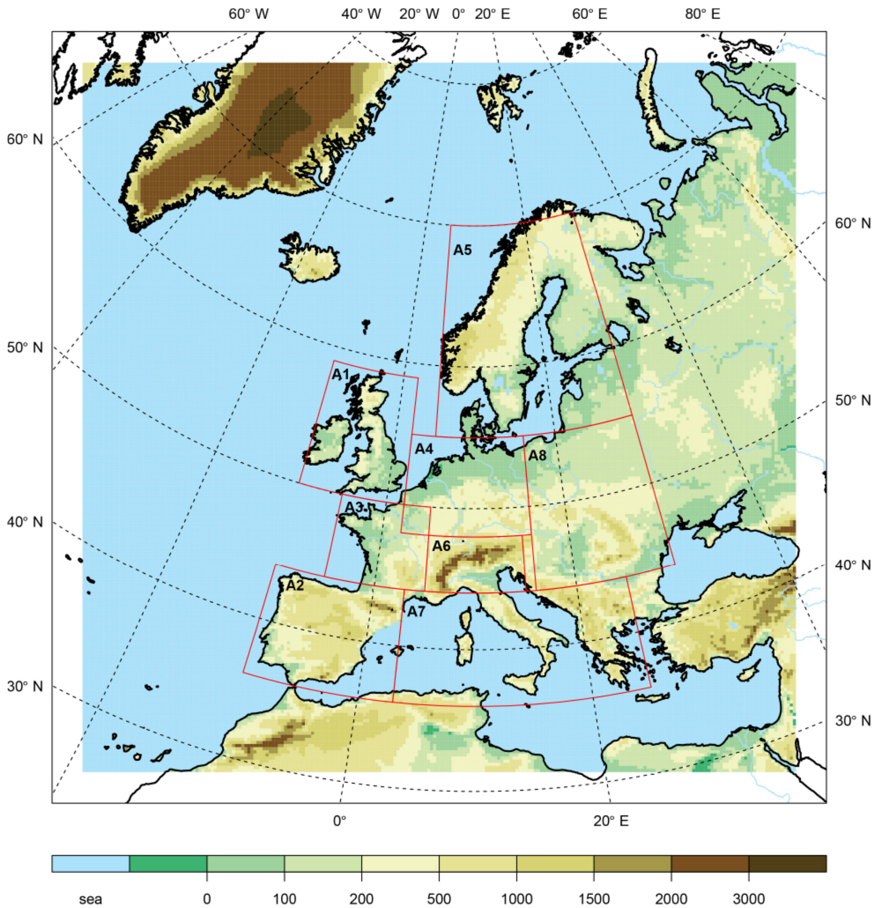

Fig. 1. Orography [m] of model domain of CCLM (colored area). The white frame indicates the 10 pixel wide sponge zone. The red boxes define the borders of the 8 European standard evaluation domains defined by Rockel and Woth (2007).

ESSDD
6, 779–809, 2013

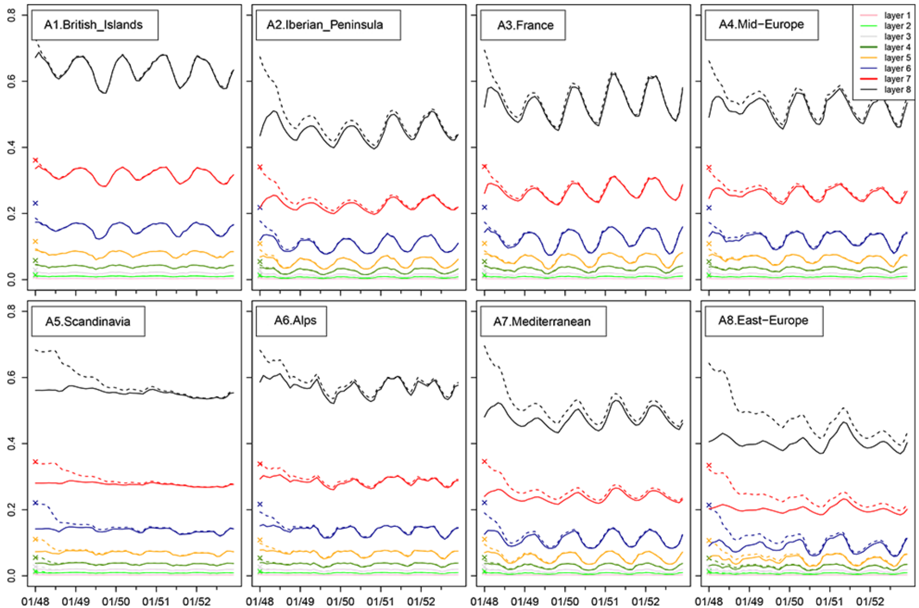

Fig. 2. Soil moisture content [m] for the 8 European sub-regions of Fig. 1. crosses: initial value, dashed lines: monthly mean of spin up run, solid: monthly mean of the final (restarted) simulation. The colors belong to the soil levels.

ESSDD
6, 779–809, 2013

High resolution atmospheric reconstruction: coastDat2

B. Geyer

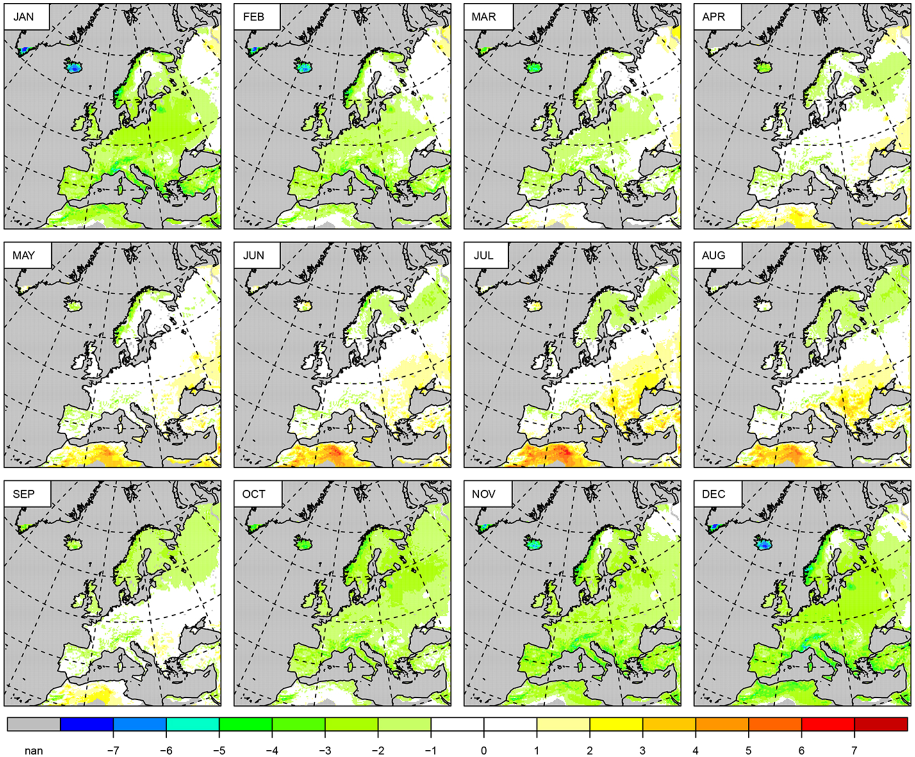

Fig. 3. Mean differences of monthly mean 2 m air temperatures [K] of 1950–2012: coastDat2-eObs8.0.

ESSDD
6, 779–809, 2013

High resolution atmospheric reconstruction: coastDat2

B. Geyer

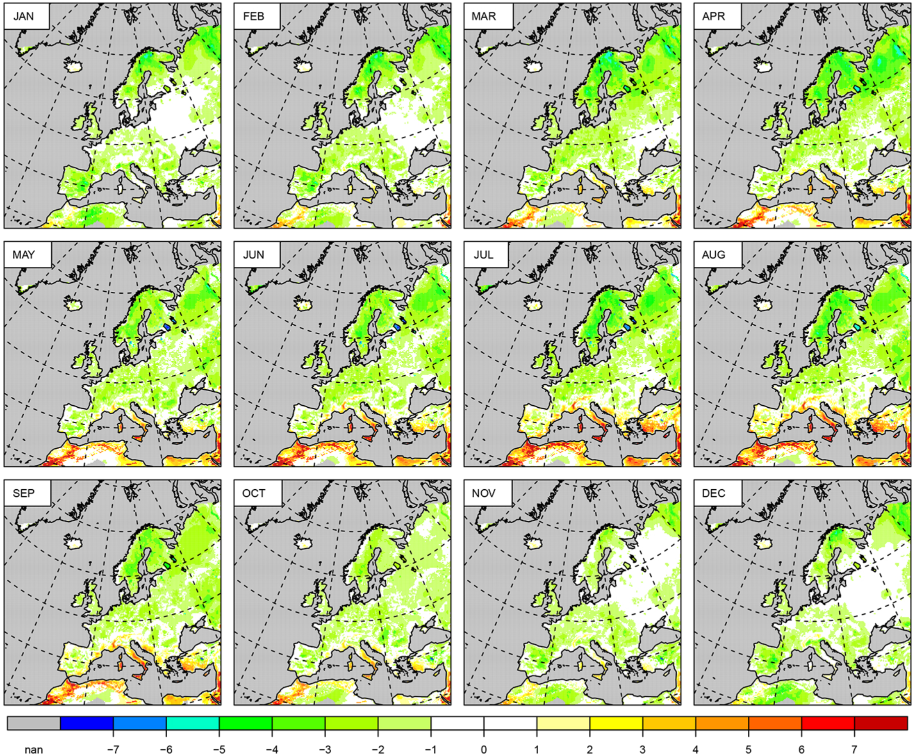

Fig. 4. Differences of mean diurnal temperature range [K] of 1950–2012: coastDat2-eObs8.0.

ESSDD
6, 779–809, 2013

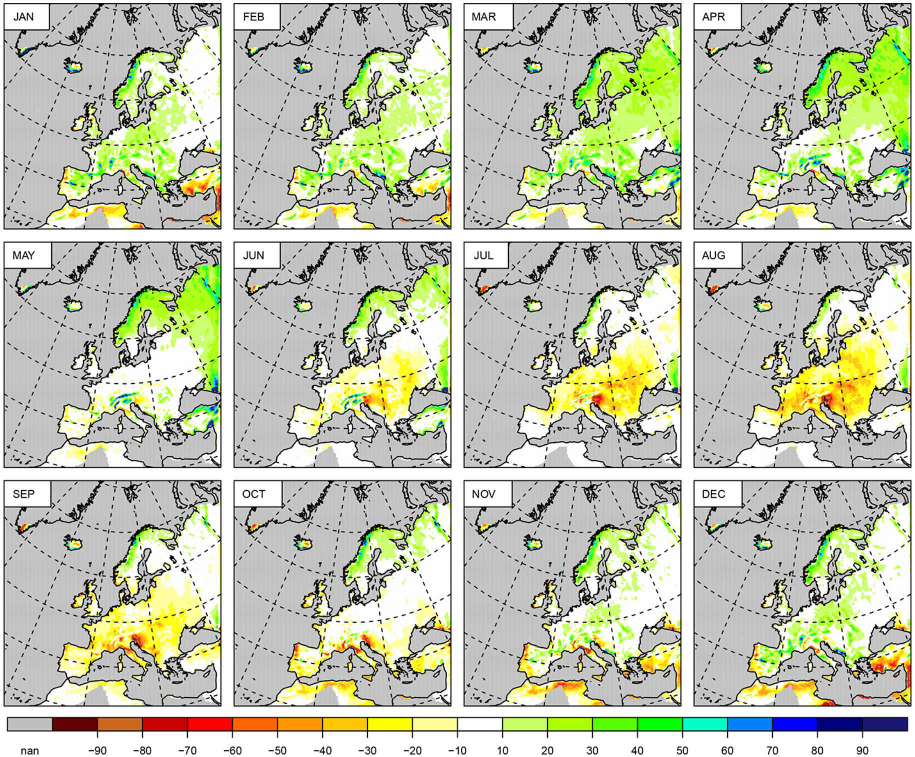

Fig. 5. Differences of mean monthly sums of total precipitation [mm] of 1950–2012: coastDat2-eObs8.0.

ESSDD
6, 779–809, 2013

High resolution atmospheric reconstruction: coastDat2

B. Geyer

Title Page
Abstract | Instruments
Data Provenance & Structure
Tables | Figures
◄ | ►
◄ | ►
Back | Close
Full Screen / Esc
Printer-friendly Version
Interactive Discussion

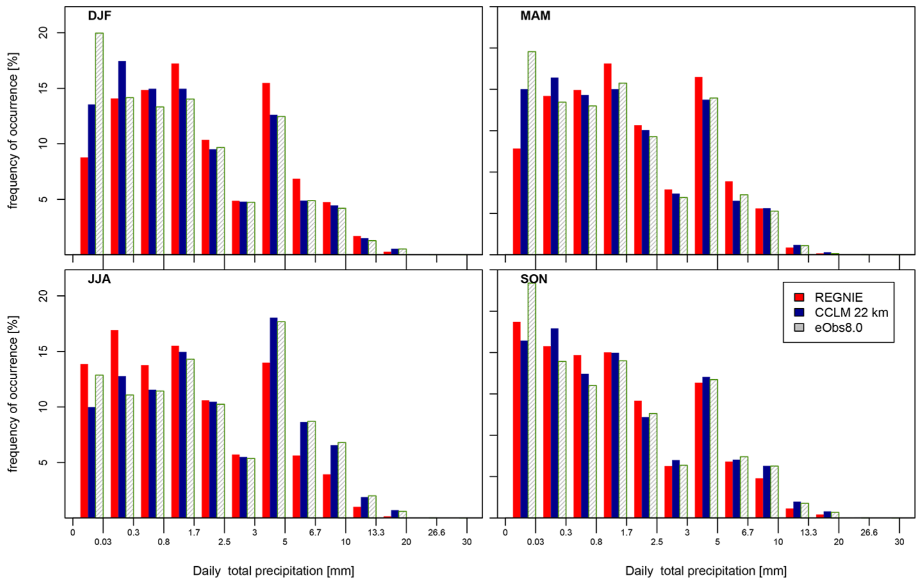

Fig. 6. Histogram of daily precipitation sums [mm] of 1951–2009: REGNIE (red bars), coastDat2 (blue bars), and eObs8.0 (shaded).The frequency is given in %.

ESSDD
6, 779–809, 2013

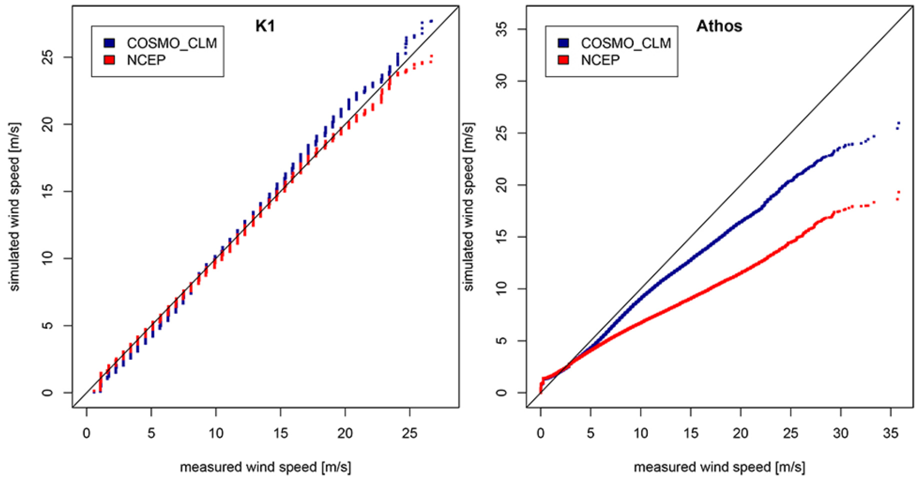

Fig. 7. Validation of near surface wind speeds: quantile-quantile plot for Atlantic offshore conditions (left: 2007–2012, platform K1 height corrected) and near-shore Mediterranean conditions (right: 2000–2012, buoy Athos).

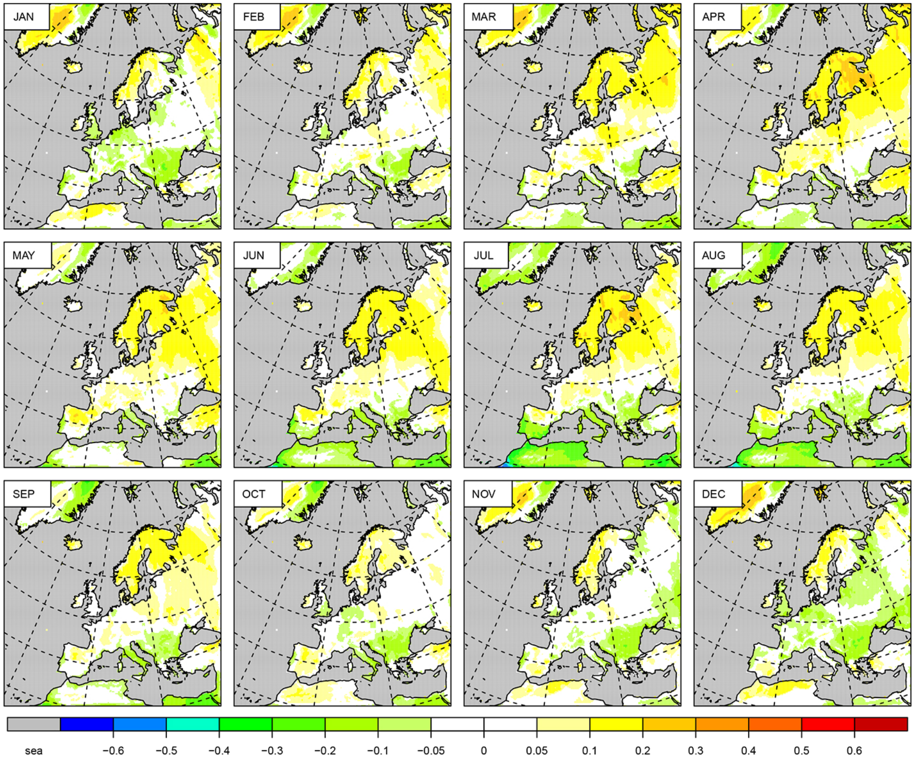

Fig. 8. Differences of mean monthly means of total cloud cover [1] of 1950–2010: coastDat2-CRU3.2.

ESSDD

6, 779–809, 2013

High resolution atmospheric reconstruction: coastDat2

B. Geyer

Title Page
Abstract Instruments
Data Provenance & Structure
Tables Figures
◀I ▶I
◀ ▶
Back Close
Full Screen / Esc
Printer-friendly Version
Interactive Discussion

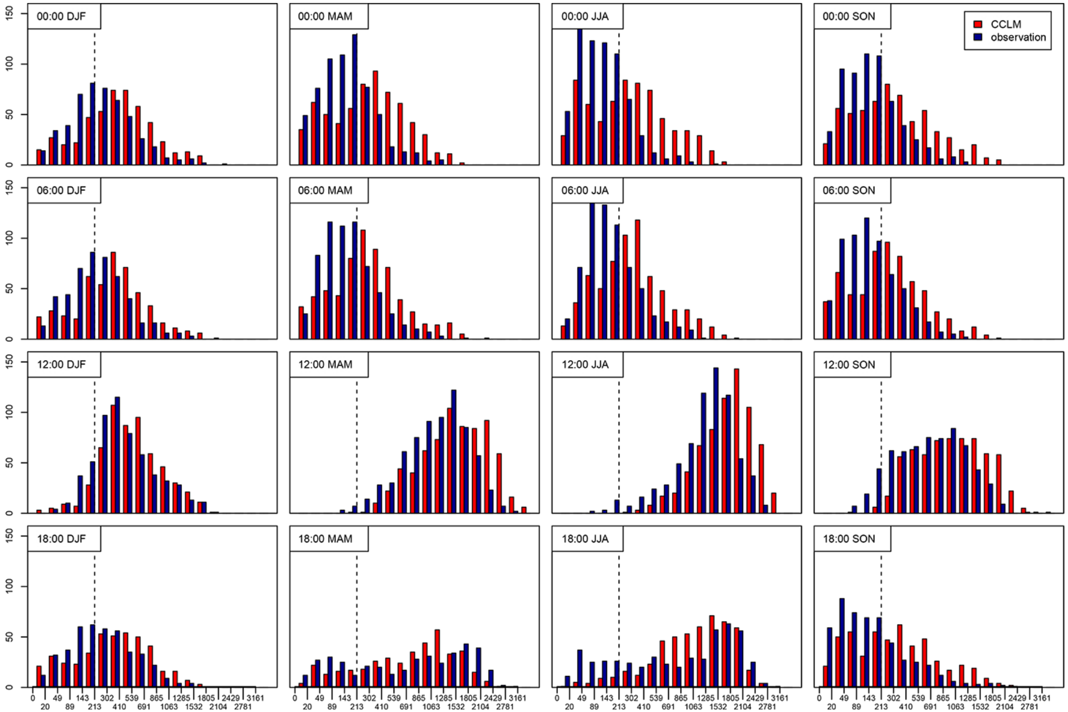

Fig. 9. Frequency distribution of the planetary boundary layer height [m] of coastDat2 and observation for 2003–2012.

ESSDD
6, 779–809, 2013

High resolution atmospheric reconstruction: coastDat2

B. Geyer

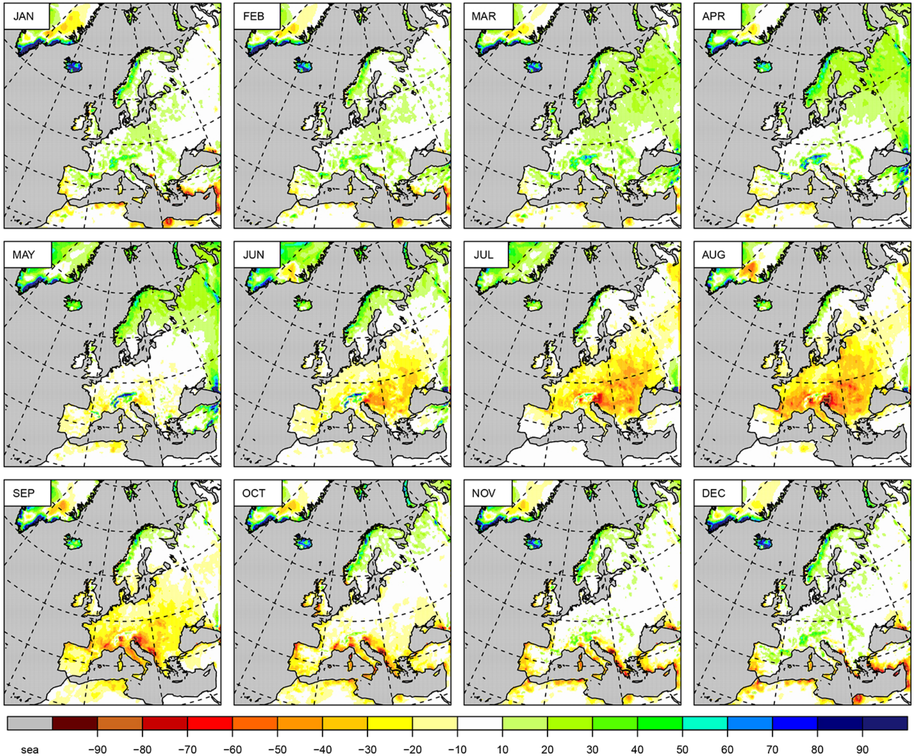

Fig. 10. Differences of mean monthly sums of total precipitation [mm] of 1950–2010: coastDat2-GPCC6.

ESSDD
6, 779–809, 2013

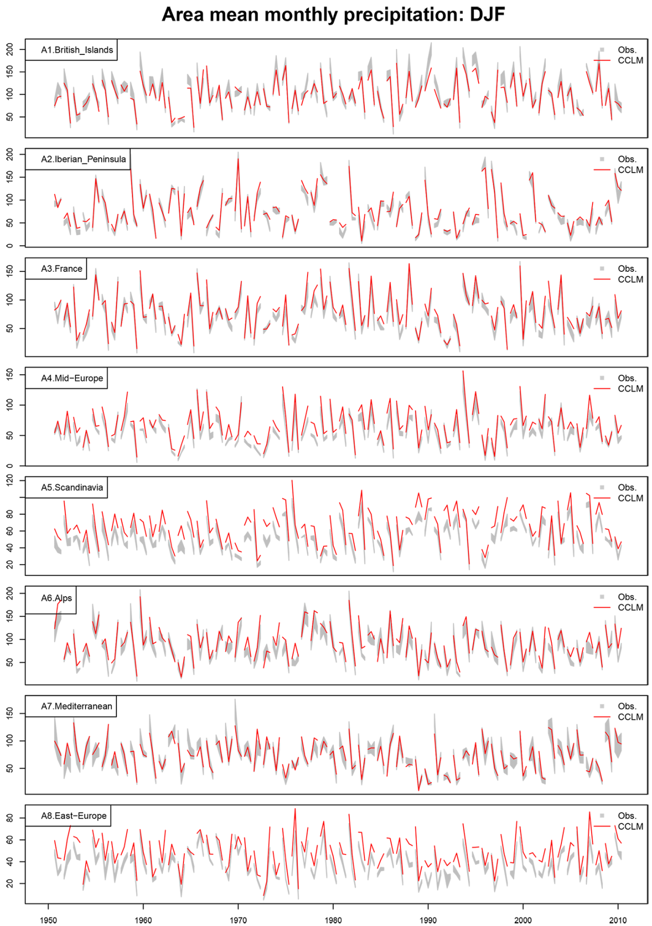

Fig. 11a. Area mean monthly sums of total precipitation of December, January, and February of 1950–2010: coastDat2 (red), range of GPCC6, eObs8.0 and CRU3.2 for each season (gray filled).

ESSDD
6, 779–809, 2013

High resolution atmospheric reconstruction: coastDat2

B. Geyer

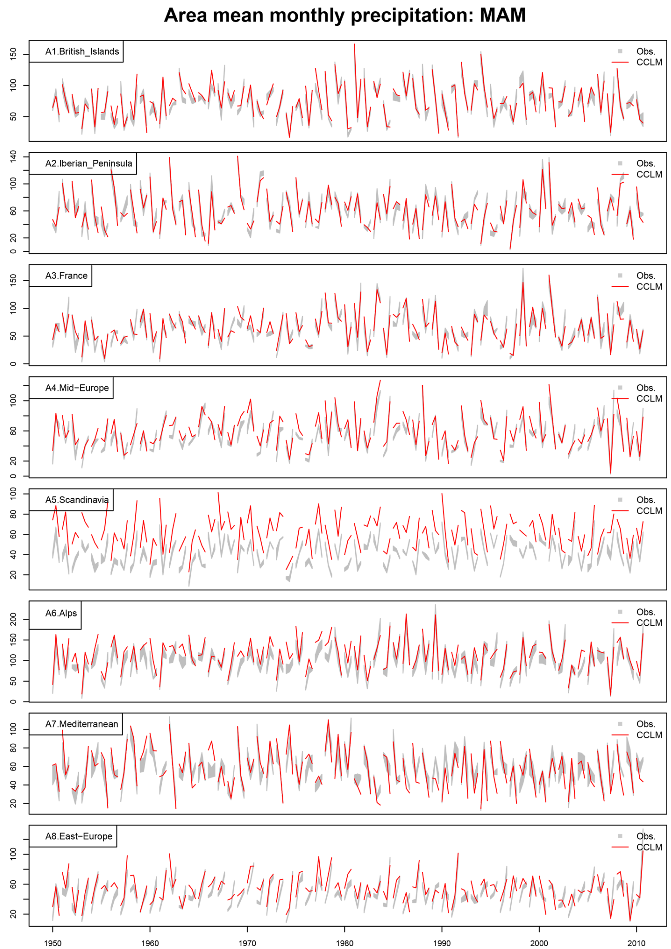

Fig. 11b. Area mean monthly sums of total precipitation of March, April, and May of 1950–2010: coastDat2 (red), range of GPCC6, eObs8.0 and CRU3.2 for each season (gray filled).

ESSDD
6, 779–809, 2013

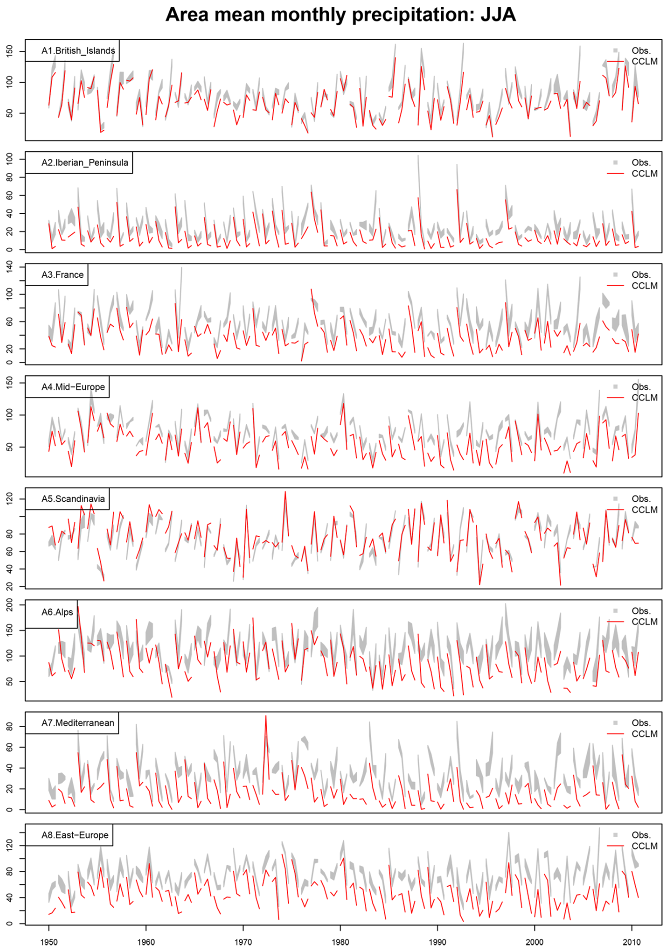

Fig. 11c. Area mean monthly sums of total precipitation of June, July, and August of 1950–2010: coastDat2 (red), range of GPCC6, eObs8.0 and CRU3.2 for each season (gray filled).

ESSDD
6, 779–809, 2013

High resolution atmospheric reconstruction: coastDat2

B. Geyer

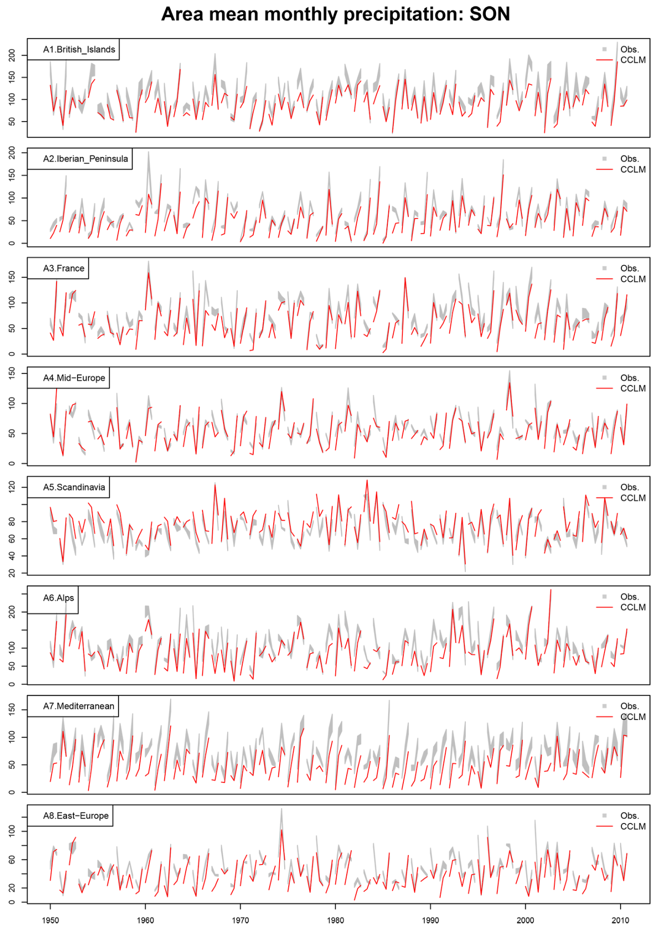

Fig. 11d. Area mean monthly sums of total precipitation of September, October, and November of 1950–2010: coastDat2 (red), range of GPCC6, eObs8.0 and CRU3.2 for each season (gray filled).

ESSDD

6, 779–809, 2013